Journal of Structural Geology 37 (2012) 75–88

Contents lists available at SciVerse ScienceDirect

Journal of Structural Geology

journal homepage: www.elsevier.com/locate/jsg

Pinch-and-swell structure and shear zones in viscoplastic layers

Stefan M. Schmalholz*, Xavier Maeder

Institute of Geology and Palaeontology, University of Lausanne, 1015 Lausanne, Switzerland

ARTICLE INFO

Article history:
Received 6 July 2011
Received in revised form
27 January 2012
Accepted 28 January 2012
Available online 4 February 2012

Keywords:
Pinch-and-swell structure
Low-temperature plasticity
Shear zones
Strain localization
Necking
Boudinage

ABSTRACT

Two-dimensional finite element simulations are presented for the extension of stiff viscoplastic layers embedded in a weaker viscous matrix. Layers and matrix exhibit power-law flow laws and the layers exhibit additionally a von Mises yield stress. The power-law flow law applies to rock deformation in the diffusion and dislocation creep regime and the von Mises plasticity to the low-temperature plasticity regime (e.g. dislocation glide). Simulations show that pinch-and-swell structure forms for small viscosity ratio (i.e. 10–20) and typical power-law stress exponents (i.e. 1–5). The pinches in layers with initial random geometrical perturbation form consecutively (i.e. not simultaneous). In multilayers, pinches on both the single-layer- and the multilayer-scale develop. Furthermore, shear zones develop due to the oblique linkage of pinches across the multilayer. These shear zones have a stable position, cause a normal drag geometry and exhibit significant displacement. The numerical results and the importance of low-temperature plasticity are supported by field observations, microstructural observations and EBSD orientation maps for pinch-and-swell structure in calcite veins. The presented models can explain strain localization by shear zone formation during bulk pure shear extension of viscoplastic multilayers without any material softening or feed-back mechanism (e.g. shear heating).

1. Introduction

Pinch-and-swell structure (Fig. 1) can form during the layer-parallel extension of a stiff viscous layer embedded in weaker viscous layers, referred to here as matrix (e.g. Ramberg, 1955; Smith, 1977; Neurath and Smith, 1982; Price and Cosgrove, 1990). The process of strain localization generating the ductile pinches in the layer is often termed necking (e.g. Price and Cosgrove, 1990). Theoretical analysis based on continuum fluid dynamics showed that pinch-and-swell structure cannot form in a layer exhibiting a linear viscous (Newtonian) rheology, but only in a layer exhibiting a non-linear viscous rheology, such as for example described by a power-law flow law with a power-law stress exponent, n, larger than one (e.g. Smith, 1977; Emerman and Turcotte, 1984; Johnson and Fletcher, 1994; Pollard and Fletcher, 2005). Analytical and numerical results further showed that viscosity ratios, R, between layer and matrix must be considerably larger than about 20 and $n > \sim 10$ so that pinch-and-swell structure develops within a reasonable amount of extension, say less than about 200% (Schmalholz et al., 2008).

The actual value of R that was present during the formation of natural pinch-and-swell structure is not easy to constrain but may often be within a range of about 10–100, which is an estimate based on analysis of single-layer folds (e.g. Hudleston and Treagus, 2010 and references therein). On the other hand, basically all values of n determined from laboratory rock deformation creep experiments for the dislocation creep, the diffusion creep and the grain-boundary sliding regime are less than 10 and typically below about 5 (e.g. Carter and Tsenn, 1987; Kohlstedt, 2007). If values of n would indeed always be smaller than 10, or even 5, for rock, then the fluid dynamic theory using power-law flow laws could not explain the formation of pinch-and-swell structure for moderate to small viscosity ratios (say <50). This limitation has been suggested in some studies where viscosity ratios in nature are mainly small ($< \sim 20$) and values of n are smaller than about 5 and, consequently, softening mechanisms, such as for example, strain-rate softening caused by chemical reactions, are essential for the formation of pinch-and-swell structure for small viscosity ratios (e.g. Hobbs et al., 2010). The term softening refers here to the applied constitutive equation (or flow law) which controls the evolution of stress and one can distinguish: (1) strain-rate softening that is a decrease of stress with increasing strain-rate and (2) strain softening that is a decrease of stress with increasing strain. In both cases, the softening is described by the applied flow law for the material behavior and is usually termed material softening. This material softening is different to the so-called structural softening that arises due to the development of structural instabilities and can also occur for linear viscous materials (e.g. Schmalholz et al.,

* Corresponding author.
E-mail address: stefan.schmalholz@unil.ch (S.M. Schmalholz).

0191-8141/$ – see front matter © 2012 Elsevier Ltd. All rights reserved.
doi:10.1016/j.jsg.2012.01.026

Fig. 1. a) Pinch-and-swell structure in layers of calc-silicate embedded in coarse-grained calcite marble (Monte Frerone, Adamello, Northern Italy). b) Pinch-and-swell structure in calcite vein in limestone (Doldenhorn nappe at Gemmipass, Leukerbad, Central Switzerland).

2005). If material softening is essential to generating pinch-and-swell structure, then pinch-and-swell structure would be a direct indicator for softening mechanisms in deformed rock, which would be important because it is usually difficult to find direct evidence for material softening in naturally deformed rock. This study investigates if pinch-and-swell structure can form for small viscosity ratios without any material softening.

It is well established by laboratory experiments of rock deformation and theoretical analysis that for lower temperature and correspondingly higher stress the power-law flow law representing dislocation creep (i.e. $n = \sim 3–5$) fails to fit the laboratory creep data (i.e. so-called power-law breakdown) and that an exponential flow law better explains the creep data (e.g. Tsenn and Carter, 1987; Kohlstedt, 2007). The stress at which the power-law breaks down for rock can be roughly estimated by dividing the rock's shear modulus by hundred, what yields several hundreds of MPa for most rocks (Tsenn and Carter, 1987). The deformation behavior at lower temperatures and higher stresses is often termed low-temperature plasticity and for silicate minerals is accomplished by dislocation glide (Kohlstedt, 2007 and references therein). The dislocations must overcome the resistance of the lattice itself which is often referred to as the Peierls barrier (Kohlstedt, 2007). Low-temperature plasticity has been experimentally observed in coarse-grained dolomite (Davis et al., 2008), clinopyroxenite (Kirby and Kronenberg, 1984) and olivine (Goetze, 1978). For Carrara marble, the power-law flow law breaks down for stresses above

~100 MPa and exponential flow laws for low-temperature plasticity can describe the deformation of Carrara marble for the high stress regime (Schmid et al., 1980), which requires effective (or apparent) stress exponents significantly larger than 10 (Schmalholz and Fletcher, 2011). These results agree with torsion experiments on Carrara marble at 500 °C that provided values of n between 25 and 17 for shear strains between 1.5 and 4, respectively (Barnhoorn et al., 2004). From a strict mathematical point of view, high stress experimental creep data can be equally well fitted with either a power-law flow law or an exponential flow law, however, values of n are then usually significantly larger than 10. For example, values of $n = 49 \pm 7$ were measured for coarse-grained Madoc dolomite (Davis et al., 2008) and $n = \sim 83$ were measured for clinopyroxenite (Kirby and Kronenberg, 1984). Schmalholz and Fletcher (2011) showed that the linearized forms of the power-law and exponential flow laws are identical and they derived formulas for the effective viscosity and n corresponding to the exponential flow law. For example, the effective power-law stress exponents, n, for the exponential flow laws determined for Jadeite and Diopside (Dorner and Stockhert, 2004) can be calculated by the method of Schmalholz and Fletcher (2011), which provides for both Jadeite and Diopside values of n ranging from about 25 to 60 for corresponding temperatures ranging from about 600 to 200 °C (larger values of n correspond to smaller values of temperature). For calcite deformation, experimental results indicate that an exponential flow law is more suitable than a power-law flow law at low-temperature and that the apparent power-law stress exponent can be significantly larger than 10 for higher stresses (>~50 MPa, Renner and Evans, 2002). Also, Renner et al. (2007) found experimentally that for two-phase marbles, the strength becomes rather strain-rate insensitive toward high stresses and large grain size. They determined apparent values of n of up to 20. With these effective (or apparent) values for n the fluid dynamic analytical solutions for folding and necking (derived for power-law flow laws, Smith, 1977) can also be applied to exponential flow laws, which not only have been applied to describe low-temperature plasticity, but also pressure solution (e.g. Rutter, 1976; Gratier et al., 2009). The high effective values of n (>10) determined for the low-temperature plasticity regime indicate an extremely weak dependence of differential stress on strain-rate and therefore, the deformation behavior for large n can be approximated with a von Mises plasticity (e.g. Kaus and Podladchikov, 2006). Von Mises plasticity provides a constant stress for all strain-rates and strains (i.e. $n \rightarrow \infty$) and therefore, is not a softening behavior (Fig. 2). Also, Turcotte and Schubert (1982) showed that a perfect plasticity model, such as von Mises plasticity, is a good approximation for the high stress deformation behavior of rock.

In this study, two-dimensional (2D) numerical simulations based on the finite element method are performed for the extension of a layer exhibiting a power-law viscous rheology and a von Mises yield stress that is embedded in a matrix with power-law viscous rheology. The stress in the layer is initially slightly below the von Mises yield stress and initial small perturbations either in the layer geometry or in the layer viscosity cause a local stress increase and, therefore, local plastic yielding. The change from a power-law viscous rheology to a von Mises plasticity represents the change in deformation regime from dislocation creep (or diffusion creep for $n = 1$) to low-temperature plasticity (or dislocation glide). Simulations are also performed for multilayers to investigate whether and how multilayer pinch-and-swell structure forms. Moreover, thin sections and Electron Backscatter Diffraction (EBSD) orientation maps are investigated for pinch-and-swell structure in calcite veins. The microstructural observations indicate low-temperature grain-boundary migration and subgrain rotation, which is achieved by dislocation glide and cross slip, consistent with plastic behavior.

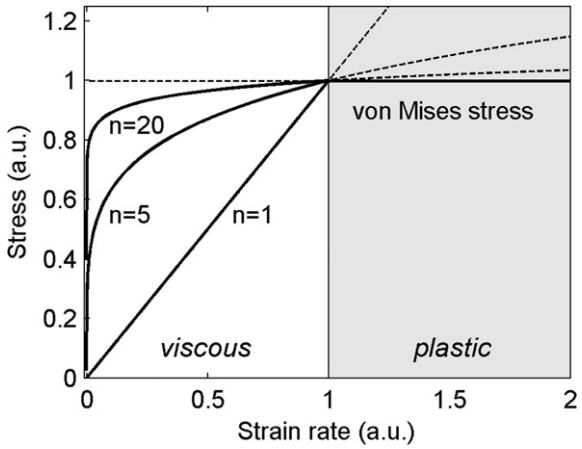

Fig. 2. Sketch of the applied stress versus strain-rate curve for a material with power-law flow law and a von Mises yield stress. Numbers are in arbitrary units (a.u.). The power-law flow law was calculated for three power-law stress exponents, n. The power-law flow law is used to model dislocation creep (e.g. $n = 5$) or diffusion creep ($n = 1$) and the von Mises plasticity is used to model low-temperature plasticity (or dislocation glide).

The main aims of this study are (1) to show that fluid dynamic models including von Mises plasticity but without any material softening can explain the formation of pinch-and-swell structure for small viscosity ratios, (2) to show that low-temperature plasticity is a rock deformation behavior which can explain the formation of pinch-and-swell structure, (3) to show that shear zones exhibiting significant displacement can form in viscoplastic multilayers and (4) to show that significant strain localization can occur without any material softening or feed-back mechanism (e.g. shear heating).

2. Numerical model

The equations of continuum mechanics describing the conservation of linear momentum (i.e. force balance equations) for slow viscous flow without gravity in 2D are (e.g. Batchelor, 1967)

$$\begin{aligned} \frac{\partial \sigma_{xx}}{\partial x} + \frac{\partial \tau_{xy}}{\partial y} &= 0 \\ \frac{\partial \tau_{xy}}{\partial x} + \frac{\partial \sigma_{yy}}{\partial y} &= 0 \end{aligned} \tag{1}$$

where x and y are the horizontal and vertical Cartesian coordinates, respectively, $\partial/\partial x$ and $\partial/\partial y$ indicates the partial derivative with respect to the x- and y-direction, respectively, σ_{xx} and σ_{yy} are total stresses and τ_{xy} is the shear stress. The constitutive equations for the power-law viscous rheology for incompressible fluids are (e.g. Johnson and Fletcher, 1994)

$$\begin{aligned} \sigma_{xx} &= -p + 2\eta \frac{\partial v_x}{\partial x} \\ \sigma_{yy} &= -p + 2\eta \frac{\partial v_y}{\partial y} \\ \tau_{xy} &= \eta \left(\frac{\partial v_x}{\partial y} + \frac{\partial v_y}{\partial x} \right) \end{aligned} \tag{2}$$

with

$$\eta = \eta_0 \left(\frac{E}{D} \right)^{\frac{1}{n}-1} \tag{3}$$

and

$$E = \left[\left(\frac{\partial v_x}{\partial x}\right)^2 + \frac{1}{4}\left(\frac{\partial v_x}{\partial y} + \frac{\partial v_y}{\partial x}\right)^2\right]^{\frac{1}{2}} \quad (4)$$

where p, v_x, v_y, η_0, D and E are the pressure, the horizontal velocity, the vertical velocity, a reference viscosity, a reference strain rate and the square root of the second invariant of the rate of deformation tensor, respectively (Johnson and Fletcher, 1994). The reference strain rate, D, could be included in the definition of η_0. However, D is introduced because, first, η_0 is then a normal reference viscosity in terms of units (i.e. Pa s) and can be used to define a reference viscosity ratio, R, between strong and weak layers, and, second, one can better distinguish if variations in the ratio of η between strong and weak layers are due to variations in material properties (i.e. η_0) or due to variations in the flow field (i.e. $E/D \neq 1$). Consequently, D is set in all simulations to the corresponding value of E for bulk pure shear extension. For $n > 1$, if flow perturbations lead to $E > D$ then η decreases with increasing strain-rate with respect to the reference viscosity (i.e. viscosity strain-rate softening) but the stress is still increasing with increasing strain-rate (i.e. strain-rate hardening, Fig. 2). If $E < D$ then η increases with decreasing strain-rate with respect to the reference viscosity. In our simulations, the applied power-law viscous flow law does not describe a material strain-rate softening for which the stress decreases with increasing strain-rate. Such strain-rate softening can also be investigated with power-law viscous flow laws by setting $n < 0$ (e.g. Montesi and Zuber, 2002). The non-linear power-law rheology is only notable if the deformation inside the model domain deviates from the applied bulk pure shear deformation and power-law effects do not exist if the strain-rate in the model domain is constant.

For incompressible materials the plasticity criteria of von Mises and of Tresca are identical (e.g. Yarushina et al., 2010) and the von Mises yield stress, σ_Y, is given by the square root of the second invariant of the deviatoric stress tensor

$$\sigma_Y = \tau_{II} = \sqrt{\tau_{xx}^2 + \tau_{xy}^2} \quad (5)$$

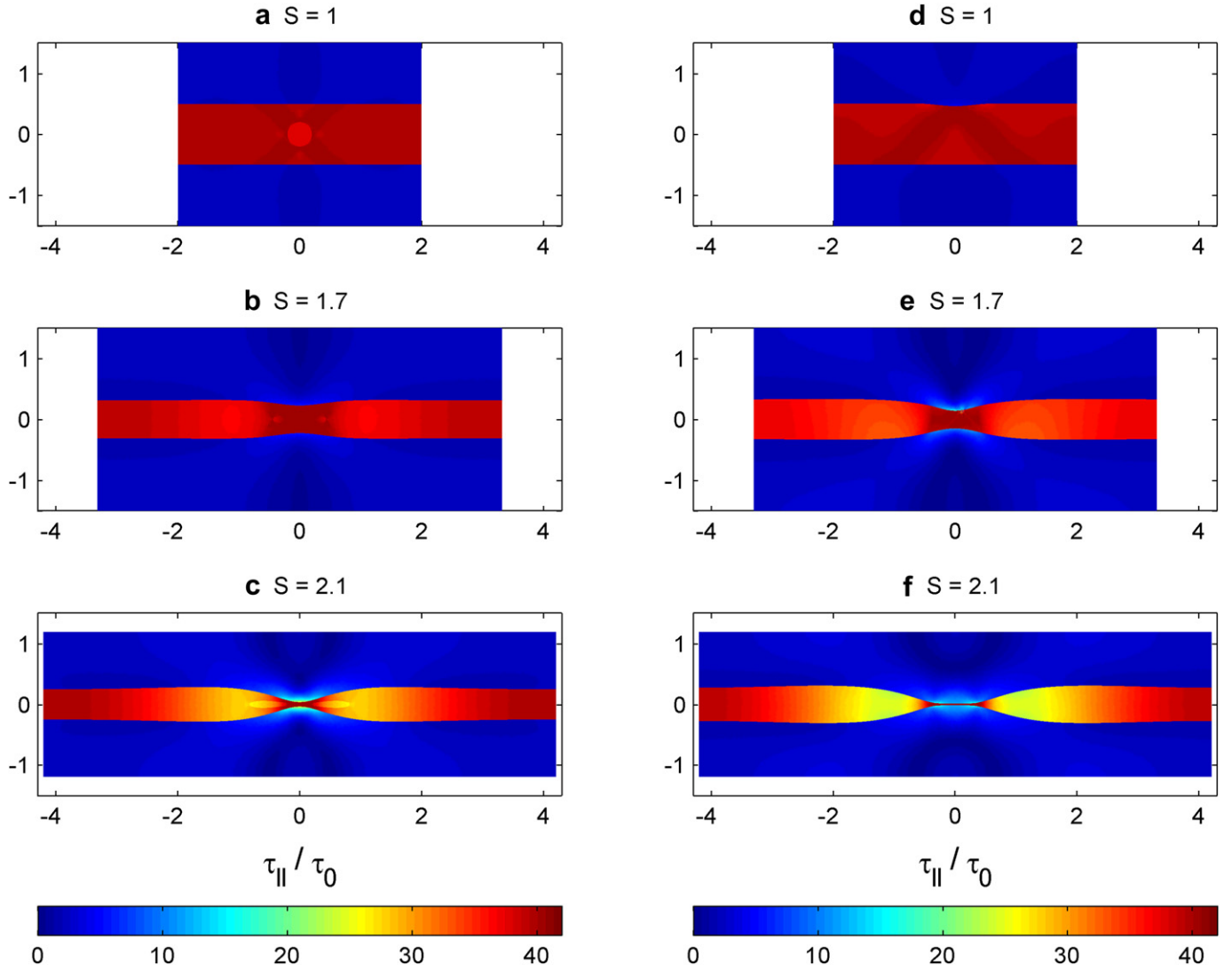

Fig. 3. Two representative numerical simulations showing the evolution of stress during the formation of pinch-and-swell structure for two models. a) illustrates the set-up for Model 1. The stiff layer is placed between two weaker layers and within the layer is a circular domain which is slightly weaker than the layer. d) illustrates the set-up for Model 2. The stiff layer is placed between two weaker layers. The layer has initially a small geometrical perturbation at the top layer boundary which makes the layer a little thinner in the middle. For both models $R = 20$, $n = 5$ and $n_1 = 1$. S is the stretch, i.e. ratio of model width to initial model width. Colors indicate the value of the square root of the second invariant of the deviatoric stress tensor, τ_{II}, which is normalized by the characteristic stress, τ_0 (i.e. product of reference viscosity of the matrix times the bulk rate of extension). a)–c) show results for model 1 and d)–f) for model 2. The dimensionless yield stress is 40.25 for both simulations.

where $\tau_{xx} = \sigma_{xx} + p$, i.e. the deviatoric stress in the horizontal direction. If viscous stresses are predicted to exceed the yield stress, i.e.

$$\tau_{II} - \sigma_Y > 0 \tag{6}$$

then the viscosity is set to

$$\eta = \sigma_Y / 2E \tag{7}$$

Therefore, the viscosity for a power-law viscous material with von Mises yield stress is

$$\begin{aligned} \eta &= \eta_0 (E/D)^{\frac{1}{n}-1} \quad \text{if} \quad \tau_{II} - \sigma_Y \leq 0 \\ \eta &= \sigma_Y / 2E \quad \text{if} \quad \tau_{II} - \sigma_Y > 0 \end{aligned} \tag{8}$$

The applied viscoplastic formulation is based on the algorithm described in Lemiale et al. (2008). The resulting stress versus strain-rate curve for a combination of a power-law flow law and a von Mises plasticity is shown in Fig. 2 (see also Pollard and Fletcher, 2005).

The applied finite element code is based on the fast solver MILAMIN (Dabrowski et al., 2008). A mixed velocity-pressure formulation is used with 7-node triangular elements (e.g. Cuvelier et al., 1986). The finite element mesh is deformed after each time step with the corresponding velocities and re-meshed with the mesh generator Triangle (Shewchuk, 2002) once the individual elements are too distorted. For each time step the viscosities are calculated iteratively. A more detailed description of the finite element algorithm can be found in Schmalholz et al. (2008).

The model set-up is illustrated in Fig. 3a and d. The numerical model domain is initially rectangular (x-direction is horizontal and y-direction is vertical) and always remains rectangular during the deformation. On all four boundaries free slip is applied. Velocity boundary conditions are applied and the velocities orthogonal to the model boundaries are modified at each time step to generate a pure shear horizontal extension of the numerical domain with a constant bulk rate of deformation (i.e. relative velocity between two model boundaries divided by the distance between these boundaries). Two basic models are considered: in model 1 (Fig. 3a) the stiff layer contains a circular inclusion in which the reference viscosity is 10% smaller than the one in the layer and in model 2 (Fig. 3d) the top layer boundary exhibits a geometrical perturbation which generates a slightly smaller layer thickness. The geometrical perturbation has a sinusoidal shape with amplitude of 1/50 of the initial layer thickness. All results are displayed in dimensionless form and the three characteristic scales are the initial layer thickness, the constant bulk rate of extension, D, and the reference viscosity in the matrix. With these three scales all model parameters are non-dimensionalized. This yields, for example, that for homogeneous pure shear deformation $E = 1$ and consequently $\eta = \eta_0$.

3. Numerical results

Fig. 3 shows two representative simulations of the formation of pinch-and-swell structure for the two models applied. The reference viscosity ratio $R = 20$, the power-law stress exponent in the layer $n = 5$ and in the matrix $n_1 = 1$. For model 1 the viscosity in the circular inclusion was 10% less than the one in the layer. The dimensionless value of τ_{II}/τ_0 (τ_0 is the characteristic stress that is the product of the reference viscosity in the matrix times the bulk rate of extension, D) is 40 in both simulations if there are no perturbations in the layer. The dimensionless value of σ_Y/τ_0 is set to 40.25, so that the layer is initially only plastically yielding in these areas that exhibit increased stresses due to the applied perturbations. Therefore, only small areas around the perturbations are plastically yielding at the onset of extension. Both simulations show that significant necking takes place and pinch-and-swell structure is well developed for a stretch, S (i.e. ratio of model width to initial model width), of about 2 (i.e. 100% extension). In both models, the layers are unloading to the left and right of the neck (pinch) at $S = 2.1$, which causes a decrease in the value of τ_{II}/τ_0. The results also indicate that the type and shape of the initial perturbation is of minor importance. However, the magnitude of the initial perturbation is important, and smaller initial perturbations generate well developed pinch-and-swell structure for larger values of S whereas larger initial perturbations generate well developed pinch-and-swell structure for smaller values of S.

The thinning factor, β (i.e. ratio of layer thickness at the neck to initial layer thickness), is plotted versus S for eight simulations in Fig. 4. For model 1, a decrease in R causes, as expected, slower thinning with extension (i.e. weaker necking instability), however, a pinch-and-swell structure is well developed also for $R = 10$ at $S = \sim 2.35$ (with $n = 5$ and $n_1 = 3$). A matrix with $n_1 = 3$ causes

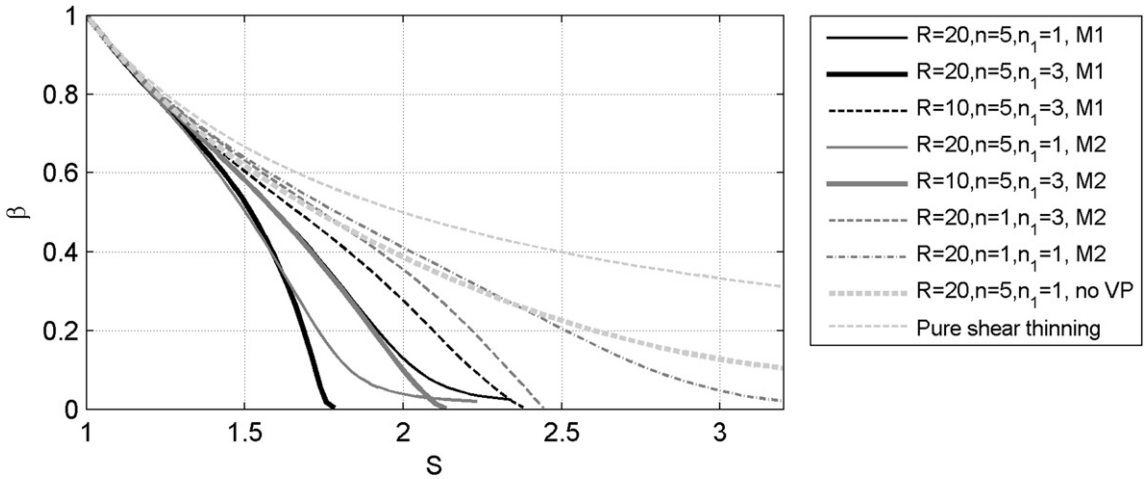

Fig. 4. The thinning factor β (i.e. ratio of layer thickness to initial layer thickness at the neck), is plotted versus the stretch, S, for eight simulations. Values of reference viscosity ratio, R, power-law exponent of the layer, n, and of the matrix, n_1, are given in the legend. M1 indicates model set-up 1 (material perturbation) and M2 indicates model set-up 2 (geometrical perturbation, see Fig. 3). The label "no VP" indicates that no von Mises plasticity was activated. For reference, the line for homogeneous pure shear thinning is also plotted.

a significantly stronger necking instability than with $n_1 = 1$ and pinch-and-swell structure is already developed for $R = 20$ at $S = \sim 1.75$ and for $R = 10$ at $S = \sim 2.1$. For all simulations where the matrix exhibited $n_1 = 3$, the thinning rate is more or less constant for very small values of β, whereas for a linear viscous matrix with $n_1 = 1$ the thinning rate slows down (Fig. 3f). Pinch-and-swell also develops if the layer is linear viscous ($n = 1$) with a von Mises yield stress and for a matrix with $n_1 = 3$. If both the layer and the matrix are linear viscous with $n, n_1 = 1$, then pinch-and-swell still develops but only for $S > 3$. If no plastic yielding is activated, then the necking instability is, as predicted by the analytical solution of Smith (1977), weak for the applied values of R, n and n_1 and no significant pinch-and-swell structure develops because thinning at the neck is only slightly faster than the background pure shear thinning of the entire layer. For the chosen parameters, the thinning for model 2 with the geometrical perturbation is faster than the thinning for model 1 for the same values of R, n and n_1. At the beginning of extension, the thinning curves for all models more or less coincide and follow the thinning curve for pure shear thinning until about $S = 1.2$. This amount of extension in the initial phase of homogeneous pure shear thinning is controlled by the magnitude of the initial perturbation. For smaller initial perturbations, the initial homogeneous pure shear thinning phase occurs over a larger range of extension, whereas for larger initial perturbations the homogeneous pure shear thinning phase occurs over a smaller range of extension and the thinning curves can diverge already from the beginning of extension.

Figs. 5–7 show three representative simulations of pinch-and-swell formation in single and multilayers with initial random geometrical perturbations of the layer boundaries. The geometrical perturbations at each numerical node of the two boundaries of each layer were generated with a random number generator and then numerically smoothed using a diffusion algorithm (Schmalholz, 2006) to generate smooth layer boundaries with initial perturbation amplitudes not exceeding 1/33 of the initial layer thickness. For the simulation shown in Fig. 5, the matrix above and below the layer has an initial dimensionless thickness of 3 (normalized by the layer thickness). The applied values were $R = 15$, $n = 3$ and $n_1 = 3$. In the early stages of extension, five pinches (the dark red areas in the layer) with more or less constant spacing initiate. This low-amplitude stage can be described with the analytical solution of Smith (1977). However, the results show that with progressive extension, individual pinches do not form simultaneously. The first pinch develops in the left part of the layer and is controlled by the applied initial perturbation. Afterward, additional pinches develop in the middle and right of the layer. Individual boudins are also extended while pinches develop to their left and right side. The stress in individual boudins strongly reduces because the high stresses are localized in the pinches. However, if the aspect ratio (i.e. ratio of length to thickness) of individual boudins is still high ($> \sim 6$), then the boudins are stressed to such an extent that new pinches can form in the center of individual large-aspect-ratio boudins. Individual boudins are stressed due to shear coupling with the matrix but not by the layer-parallel extensional stress throughout the layer. The maximal bulk extension shown in Fig. 5 is about 270%.

Fig. 6 shows a simulation with three layers with initial random geometrical perturbations for $R = 15$, $n = 5$ and $n_1 = 3$. The three layers have the same properties. The initial dimensionless thickness of the matrix above and below the three layers is 3. The initial dimensionless thickness of the bottom layer is 0.5, of the middle layer is 1 and of the top layer is 0.75. The initial dimensionless thickness of the matrix between the two lower layers is 0.5 and the one of the matrix between the two upper layers is 0.75. Pinch-and-

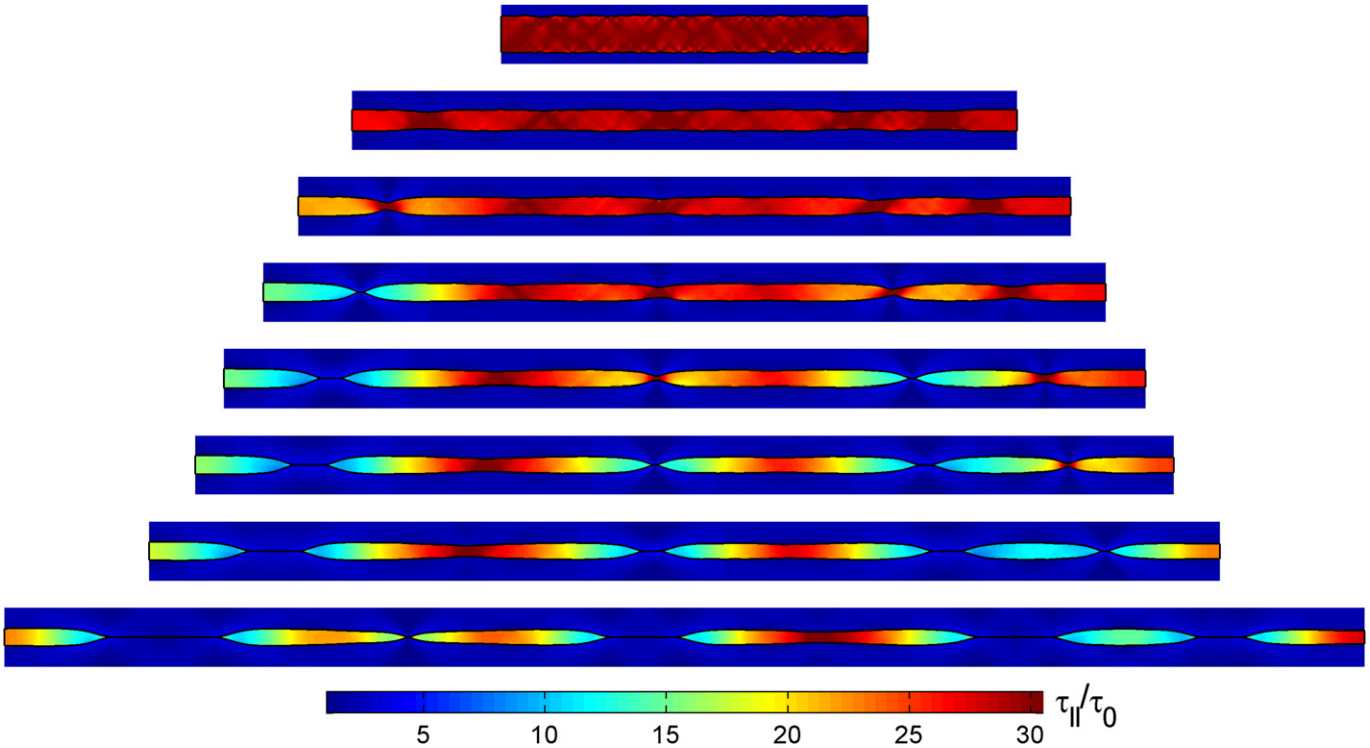

Fig. 5. Numerical simulation showing the formation of pinch-and-swell structure in a layer with initial random geometrical perturbations on the top and bottom layer boundary. $R = 15$, $n = 3$ and $n_1 = 3$. Colors indicate the value of the square root of the second invariant of the deviatoric stress tensor, τ_{II}, which is normalized by the characteristic stress, τ_0 (i.e. product of reference viscosity of the matrix times the bulk rate of extension). For better visualization, only a portion of the matrix (blue domain) is shown in the individual plots. The dimensionless yield stress is 30.25.

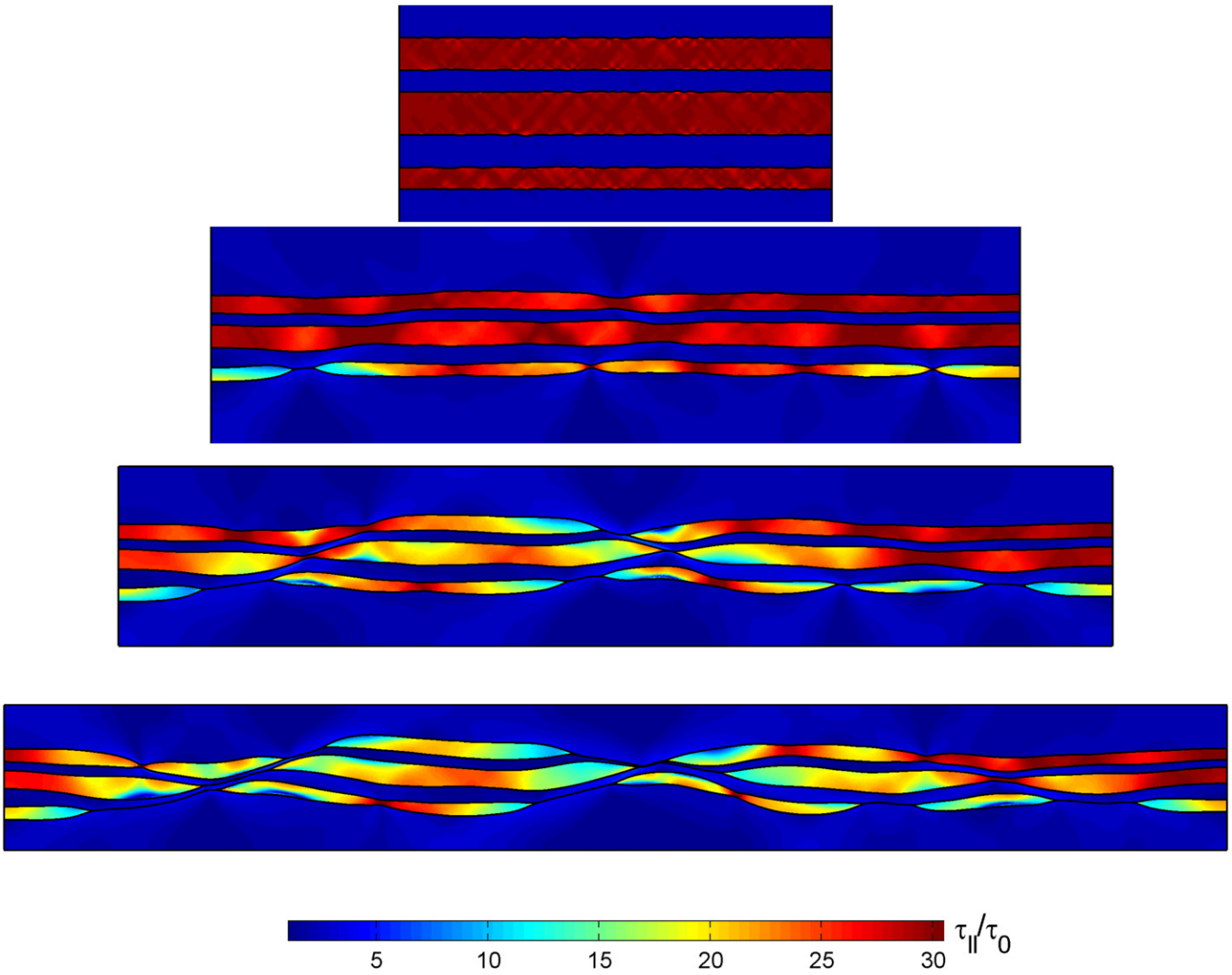

Fig. 6. Numerical simulation showing the formation of pinch-and-swell structure in three layers with initial random geometrical perturbations on the top and bottom layer boundary and with different initial thickness and spacing. $R = 15$, $n = 5$ and $n_1 = 3$ for all layers and matrix. Colors indicate the value of the square root of the second invariant of the deviatoric stress tensor, τ_{II}, which is normalized by the characteristic stress, τ_0 (i.e. product of reference viscosity of the matrix times the bulk rate of extension). For better visualization, only a portion of the matrix (blue domain) is shown in the individual plots. The dimensionless yield stress is 30.25.

swell formation is fastest in the thinnest, lower layer because for this layer the initial amplitudes are largest relative to the initial layer thickness. After some extension, the three layers start to behave as one (anisotropic) layer and develop two pinches on the scale of the multilayer. Individual boudins in individual layers are locally strongly curved. The large pinch in the left of the multilayer has the geometry of a shear zone with a normal fault shear sense (i.e. left side moves relatively down).

Fig. 7 shows a simulation with nine layers with initial random geometrical perturbations for $R = 20$, $n = 5$ and $n_1 = 3$. The dimensionless thickness of the stiff layers is always 1, the dimensionless thickness of the weak interlayers is 0.5 and the one of the bottom and top weak layer is 6. Until about 76% extension (Fig. 7c) the layers are more or less horizontal and several pinches have formed in the layers with the largest pinch in the bottom layer. At 87% extension, several pinches are oriented along two oblique shear zones across the multilayer with normal shear sense. The larger shear zone is in the right of the model and dips to the left whereas a smaller shear zone is in the left of the model and dips to the right. At 98%, the shear zones have further developed but do not transect the entire multilayer. At 137%, the shear zone in the right of the model transects the entire multilayer and considerable strain and displacement are localized along this zone. The shear zone formed due to the oblique linkage of pinches across the multilayer. Individual layers are dragged and bent into the shear zone and clearly indicate the shear sense. At 191%, the shear zone is slightly curved (convex upwards) and exhibits significant displacement. The layers surrounding the shear zone exhibit a shape termed normal drag in the context of flanking structures (e.g. Grasemann et al., 2003) or normal faulting (e.g. Grasemann et al., 2005), but this particular geometry developed during bulk pure shearing. A second smaller shear zone also developed in the left of the model. The entire multilayer has developed one pinch-and-swell structure where significant deformation occurred in a single shear zone by simple shear. This process is different to the pinch-and-swell formation in the single layers where the pinch forms due to pure shear thinning and not simple shearing. This shear zone development in the multilayer is, therefore, a true multilayer effect because such shear zones did not develop in the single-layer simulations during bulk pure shear extension.

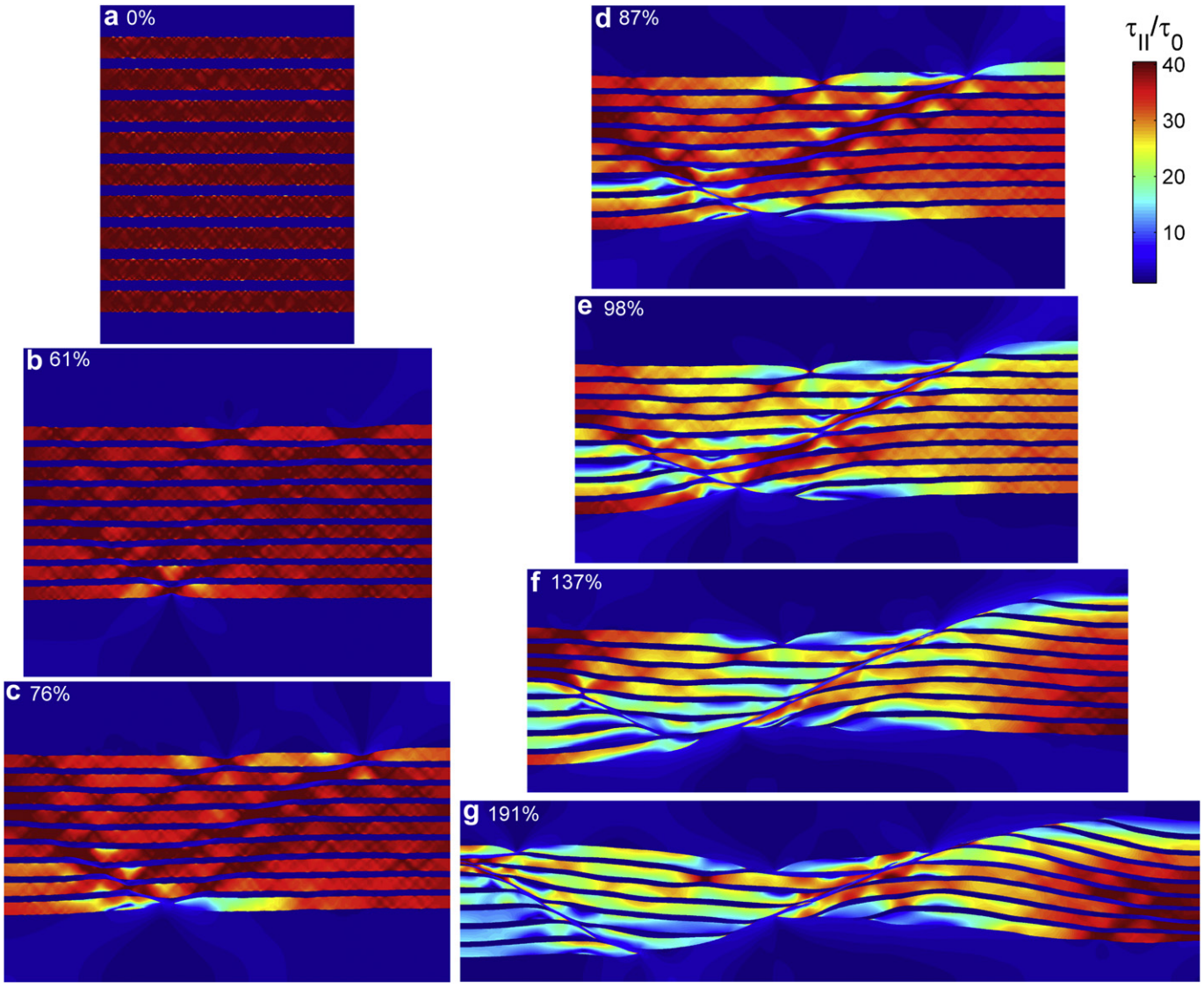

Fig. 7. Numerical simulation showing the formation of pinch-and-swell structure and shear zones in nine layers with initial random geometrical perturbations on the top and bottom layer boundary. $R = 20$, $n = 5$ and $n_1 = 3$ for all layers and matrix. Numbers indicate bulk extension in %. Colors indicate the value of the square root of the second invariant of the deviatoric stress tensor, τ_{II}, which is normalized by the characteristic stress, τ_0 (i.e. product of reference viscosity of the matrix times the bulk rate of extension). For better visualization, only a portion of the matrix (blue domain) above and below the multilayer is shown in panel a). The dimensionless yield stress is 40.25.

4. Field observations, microstructures, deformation mechanisms and flow laws

Fig. 8a and b shows two examples of single-layer pinch-and-swell structure in calcite veins in fine-grained calcite rock from the inverse limb of the Morcles fold nappe (Grand Chavalard, Western Switzerland). The calcite veins exhibit features similar to the numerically simulated pinch-and-swell structure for random initial perturbation (Fig. 5), such as for example: (1) the distance between individual boudins varies, indicating a non-simultaneous and consecutive formation of the pinches; and (2) some boudins show half-developed pinches in their middle indicating that the ductile deformation stopped before the pinch fully developed. The multilayer of calcite veins in Fig. 8c is from the same location as the calcite veins shown in Fig. 8a and b. The multilayer exhibits a shear zone with a normal shear sense that is similar to the shear zones in the numerical simulations with the multilayers (Figs. 6 and 7). The individual calcite layers in Fig. 8c also exhibit pinch-and-swell structure. The calcite layers are also slightly curved and exhibit normal drag geometry with respect to the shear zone, which is similar to the geometry of the layers around the shear zone in the simulations (Fig. 7g). A thin calcite layer above the shear zone seems to be unaffected by the shear zone indicating that the shear zone is localized around the multilayer, which is again similar to the shear zone in the numerical simulations.

Fig. 9 shows a thin section of a calcite vein in a fine-grained calcite rock from the same location as the calcite veins shown in Fig. 8. The vein exhibits a pinch-and-swell structure (Fig. 9a). The grain-size distribution in the vein is heterogeneous with large grains of several millimeters in the swell (Fig. 9a, b and d) versus about 25 μm in the pinch (Fig. 9c). In the swell, the grain interiors exhibit abundant twins, which are often smoothly bent and/or exhibit some kinks. Some twins become narrower toward the grain-boundary or have lensoid shapes (Fig. 9b), showing typical features of type III twins as described by Burkhard (1993). The bending of twins is interpreted to result from dislocation glide

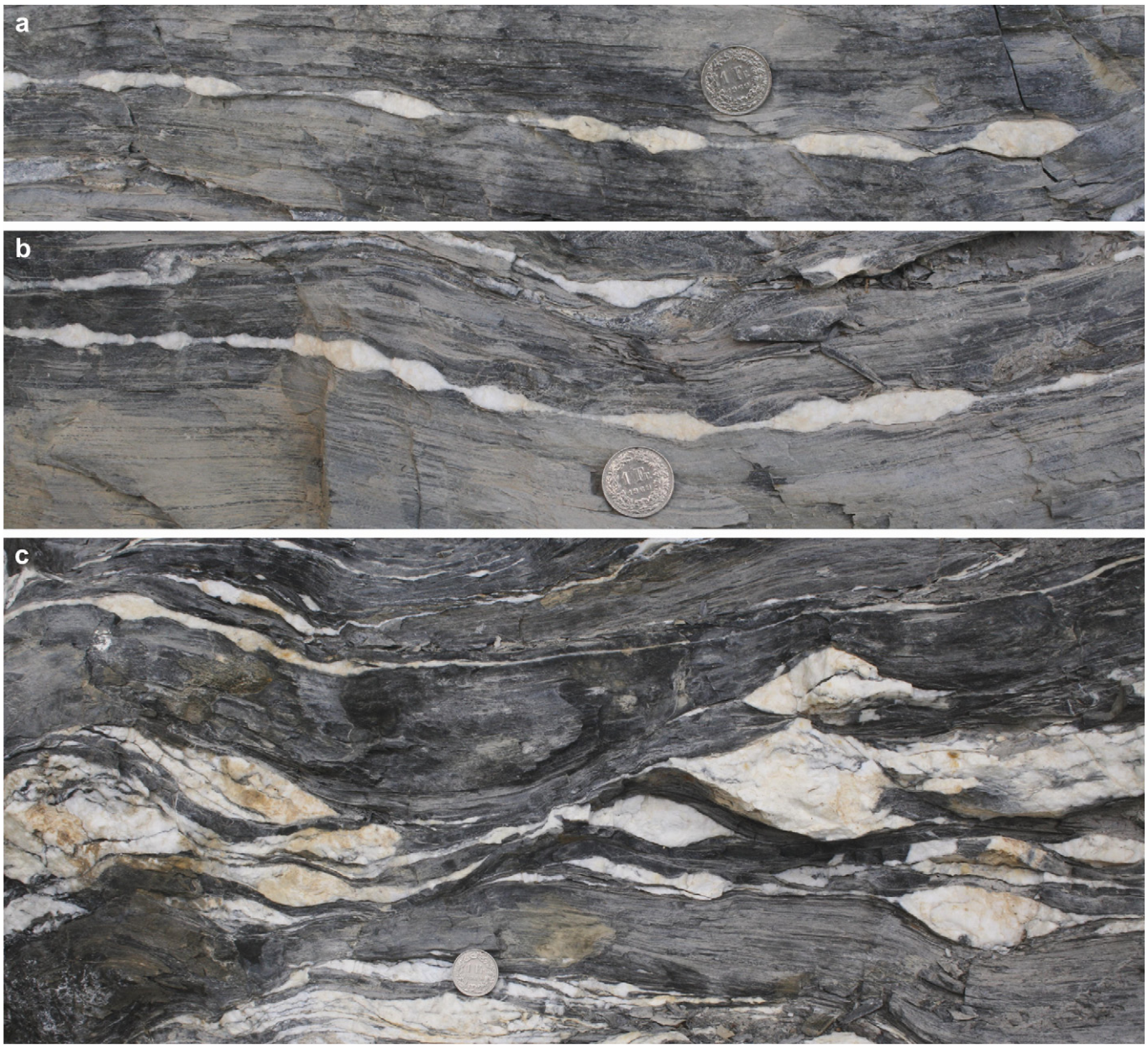

Fig. 8. a) and b) Single-layer pinch-and-swell structure in calcite veins in marble. c) Shear zone in multilayer calcite veins in marble. Individual calcite veins show pinch-and-swell structure. All photos are from the inverse limb of the Morcles nappe, Grand Chavalard, Western Switzerland.

(Burkhard, 1993). Undulose extinction is common in the larger grains. Small calcite grains of similar size (10–30 μm) surround the coarse grains and developed along the grain boundaries and some twin lamellae (Fig. 9b). The small grains are usually arranged in bands. These small grains show no undulose extinction and no twins. The average grain size within the thicker pinch (left part of Fig. 9a) is considerably larger than the grain size within the thinner pinch (Fig. 9c). Electron backscatter diffraction (EBSD) orientation map for an area in the swell of a calcite vein (from the same location as the veins in Fig. 8) shows that the grains smaller than about 30 μm, which developed between the large grains, have no internal misorientation and no subgrains, which confirms the thin sections observations (Fig. 10). Larger grains show internal misorientation gradients and subgrains based on progressive change of colors inside the grains in the EBSD map (Fig. 10). Grains larger than 1 mm show deformation bands and progressive internal misorientation of more than 30° indicating strong internal deformation that must be accommodated by dislocation arrays (Fig. 10b).

The EBSD map shows progressive increase of deformation and crystal lattice misorientation toward the border of the large grains. Subgrain boundaries form and gradually increase in misorientation until forming high angle boundaries (larger than 10°) and new grains. All these microstructures are typical for the deformation of large grains at relatively low to medium temperature and result from progressive recovery, low-temperature grain-boundary migration or bulging and some subgrain rotation processes (e.g. Hirth and Tullis, 1992; Stipp et al., 2002; Bestmann and Prior, 2003; Passchier and Trouw, 2005). The recrystallized small grains that surround the large grains are generally named mantle (sub)grains (e.g. White, 1976). The bulges separate from the host grains to form small independent new grains after subgrain formation. These processes are considered to be mainly

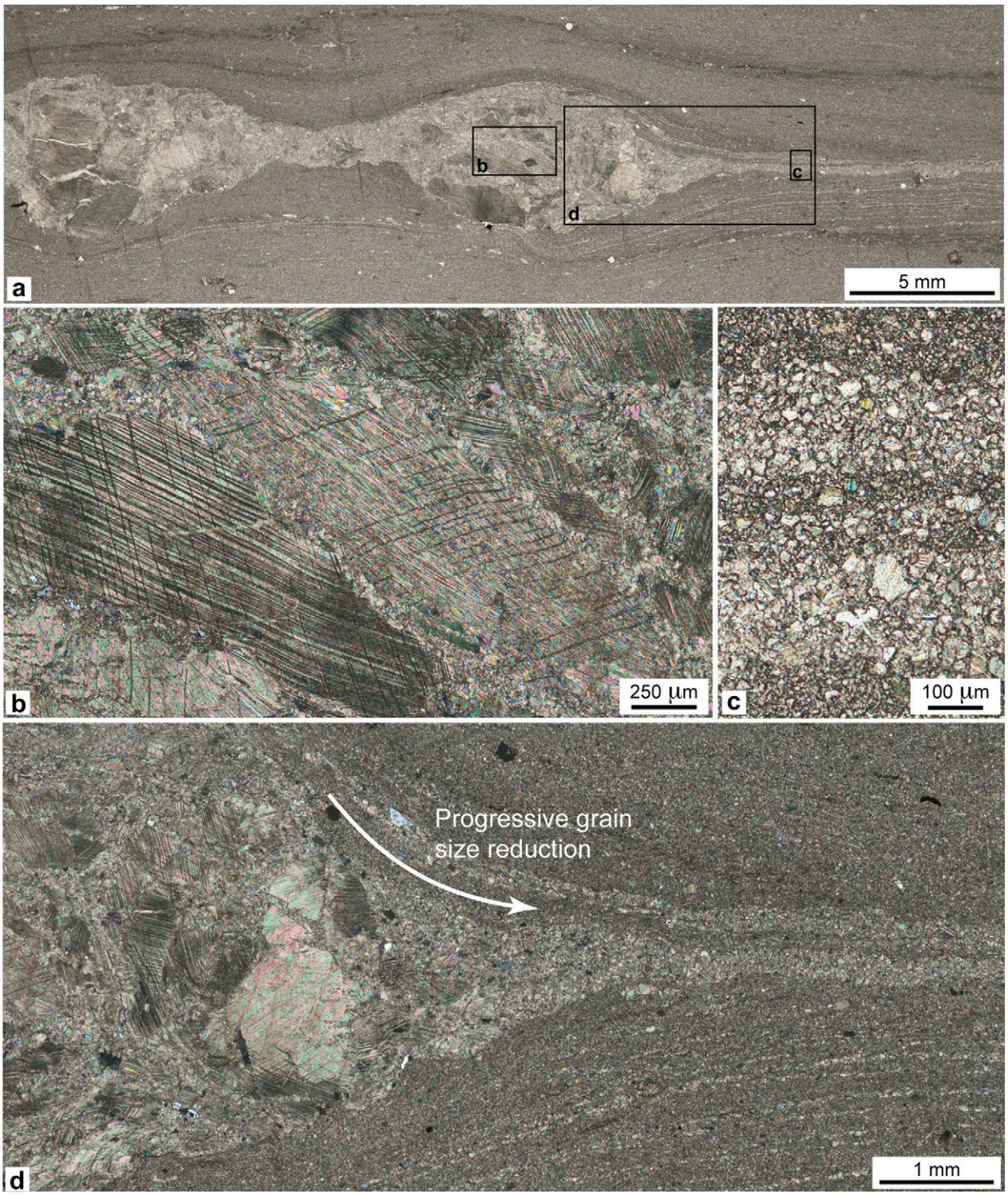

Fig. 9. Thin section pictures of a calcite vein in fine-grained calcite rock showing a pinch-and-swell structure from the same location as Fig. 8. The vein shows heterogeneous grain-size distribution with large grains of several millimeters in the swells (a, b and d) and grains of about 25 μm in the pinch (c). Progressive grain-size reduction is observed from the swell toward the pinch (a and b). Coarse grains exhibit abundant twins that are frequently bent and deformed. Subgrains are around the coarser grains due to the deformation (see text for detailed description).

controlled by dislocation glide (e.g. regime 1 of Hirth and Tullis, 1992) for the relatively low deformation temperatures for these calcite veins (around 330–350 °C, Herwegh and Pfiffner, 2005). This analysis is in agreement with work of De Bresser and Spiers (1990, 1993) and De Bresser (2002), who suggested that dislocation glide in combination with cross slip (rather than dislocation climb) is the mechanism controlling creep of calcite at low to intermediate temperature and stress. Cross slip is a process in which dislocations overcome obstacles in the glide plane by gliding onto a plane oriented oblique to the original glide plane (De Bresser, 2002). For such cross slip, values of n are larger than 10 (De Bresser, 2002).

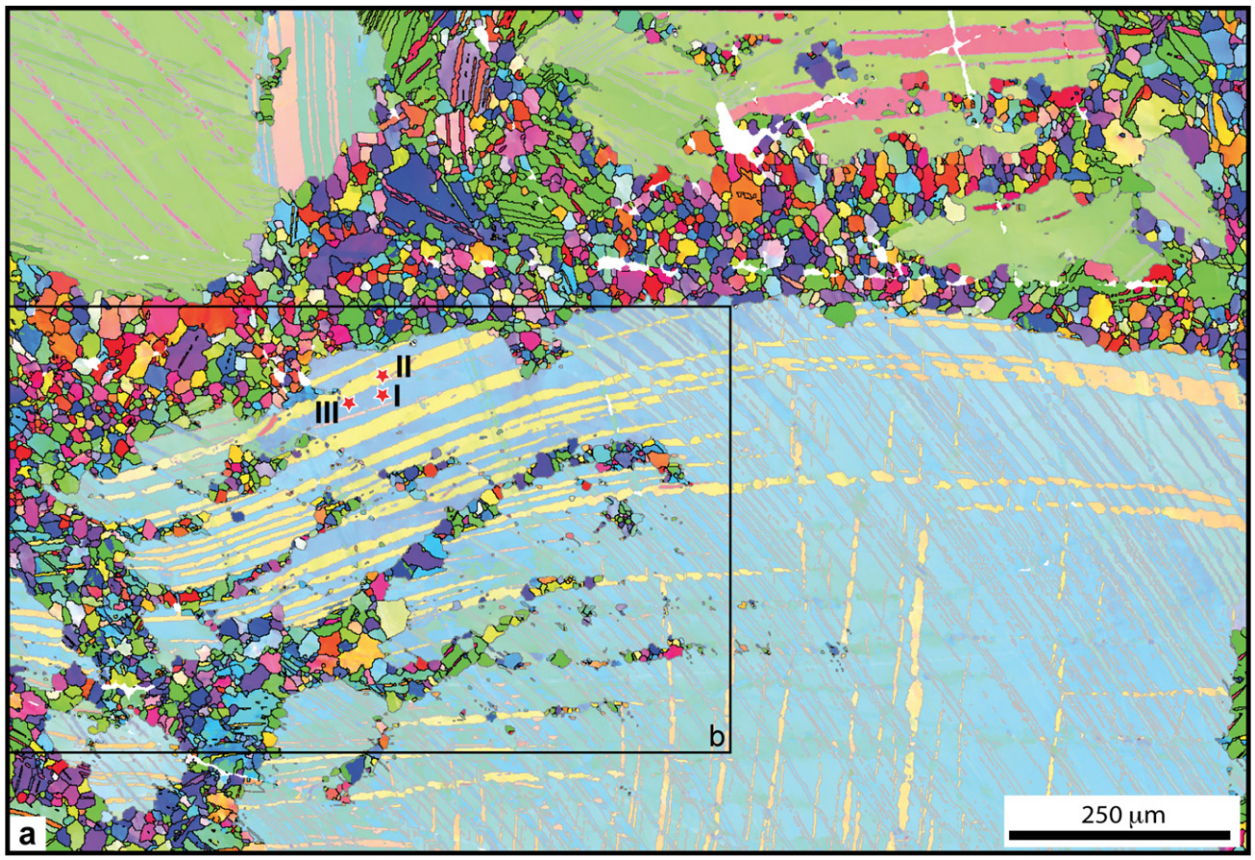
II
I
III
b
a
250 μm

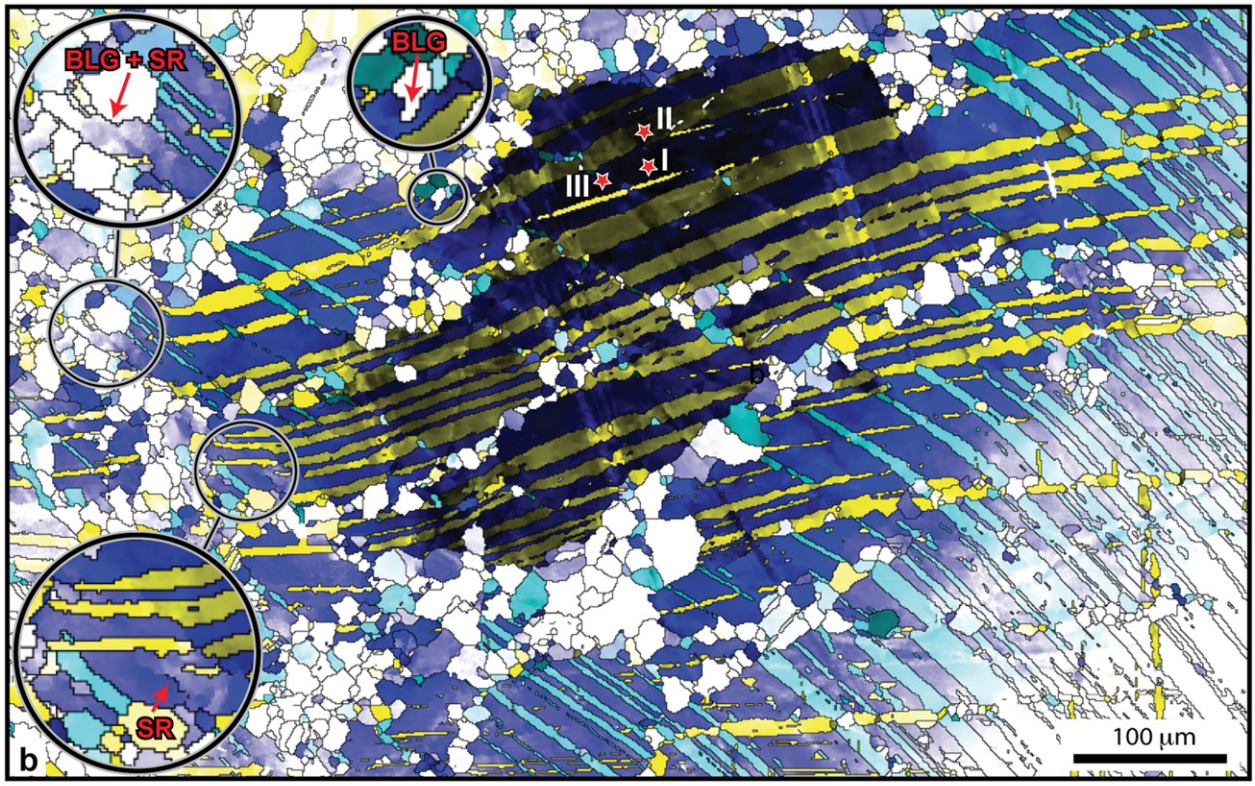
BLG + SR
BLG
II
I
III
b
SR
b
100 μm

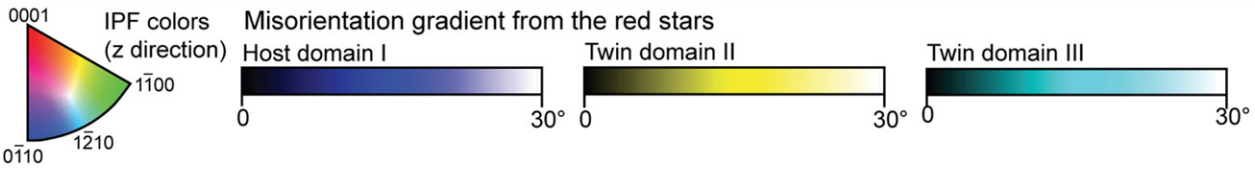
0001
IPF colors
(z direction)
1$\bar{1}$00
0$\bar{1}$10
1$\bar{2}$10
Misorientation gradient from the red stars
Host domain I
0
30°
Twin domain II
0
30°
Twin domain III
0
30°

The observed microstructures and the presence of bent twins indicate dislocation creep by mainly glide and low-temperature grain-boundary migration as the dominant deformation mechanism in the swell area and in the thicker pinch (left pinch in Fig. 9a), which was thinned by a factor of about four. Intensive grain-size reduction reduces the coarse grains in the swell to progressively smaller grains toward the pinch where the grain size is about 10 and 30 μm, which is slightly larger than the grain size in the matrix. The grains in the pinch have isotropic shape and lack undulose extinction or twins. The absence of internal deformation and the small size of the grains suggest a strong component of grain-boundary sliding accommodated by diffusion creep (or granular flow) in the pinch. Therefore, a change of deformation mechanism from dislocation creep dominated to diffusion creep dominated can occur when the pinch was already thinned considerably.

Using the exponential flow law for calcite from Renner and Evans (2002) and Renner et al. (2002) with differential stresses between 100 and 250 MPa, temperatures between 300 and 350 °C and a grain size of 1 mm provides values of the apparent stress exponent between 14 and 34 (higher values for higher stresses). These estimates suggest that (1) the stress sensitivity on strain-rate was weak in the calcite, (2) the deformation of the calcite was likely close to a perfectly plastic deformation and (3) that conditions for pinch-and-swell formation were favorable. In summary, the field observations, the microstructures, the studies on deformation mechanisms and the experimentally derived flow laws are in overall agreement and support a flow law with high effective values of n (i.e. low-temperature plasticity) to describe the deformation of the observed calcite veins.

Estimates for the deformation mechanism based on existing flow laws can also be made for the pinch-and-swell structures shown in Fig. 1. Fig. 1a shows calc-silicate layers in coarse-grained calcite marble. For such marble, many rock deformation creep experiments yield power-law stress exponents around 5 assuming a power-law flow law and dislocation creep (e.g. Carter and Tsenn, 1987). The mineral composition of the calc-silicate layers is in general highly variable but for the layers shown in Fig. 1a, the dominant minerals are likely plagioclase and diopside (Peter Brack and Lukas Baumgartner personal communication, also Brack, 1981, 1985). The temperature during the deformation has been probably around 500 ± 30 °C (Lukas Baumgartner personal communication). For 500 °C, the exponential flow law for Diopside from Dorner and Stockhert (2004) provides an effective power-law stress exponent of about 35 for a strain rate of 10^{-14} s^{-1} and of about 38 for a strain rate of 10^{-12} s^{-1}. Furthermore, Rybacki and Dresen (2004) presented deformation mechanism maps for feldspar rocks and the results show that for a temperature of 500 °C and a strain rate of 10^{-12} s^{-1} the stresses in a wet anorthite are >400 MPa. Therefore, the deformation behavior is low-temperature plasticity by dislocation glide and/or semibrittle flow. However, it is difficult to assess which flow law would most accurately describe the deformation of the calc-silicate layer. The presence of plagioclase and diopside in the layers and the temperatures around 500 °C at least indicate high effective values of n and suitable conditions for pinch-and-swell formation without the need for softening mechanisms. The pinch-and-swell structure in Fig. 1b shows a calcite vein in limestone from the Doldenhorn nappe (Gemmipass, Leukerbad, Switzerland). Maximum temperatures between 300 and 350 °C were estimated using geothermometry (Herwegh and Pfiffner, 2005). As for the calcite veins shown in Fig. 8, these temperatures and the grain sizes around 1 mm indicate effective power-law stress exponents significantly larger than 10, which can explain pinch-and-swell formation by necking instability.

5. Discussion

The calcite veins displayed in Figs. 8 and 9 likely formed with more or less constant thickness and the initial grain size in the vein was likely similar to the grain size in the swells (i.e. larger or equal around 1 mm), which presumably have been deformed least. Microstructural observations indicate that the grains deformed and progressively reduced in size toward the pinch by dynamic recrystallization. This dynamic recrystallization is due to low-temperature grain-boundary migration and subgrain rotation, which are controlled by dislocation glide and cross slip. Flow laws describing rock deformation controlled by these mechanisms exhibit, in general, values of n significantly larger than 10 and such deformation behavior is referred to here as low-temperature plasticity. Field data, microstructural observations, calcite flow laws and the numerical simulations suggest the following scenario for the formation of the pinch-and-swell structure and shear zones in the calcite veins shown in Figs. 8 and 9: (1) the calcite veins form with different thicknesses but each vein has more or less constant thickness; (2) the dominant grain size in the veins is initially larger or equal around 1 mm; (3) the calcite veins are extended parallel to the veins; (4) the deformation behavior of the calcite veins preserving near constant thickness is dominated by low-temperature plasticity; (5) the large effective stress exponents cause significant necking instabilities in the extending calcite layers; (6) during the deformation and necking the grain size is continuously reduced; (7) in closely spaced calcite veins, shear zones form due to the oblique linkage of pinches across the calcite multilayer; (8) the grain size remains large in the swells, which experience the least deformation, whereas the grain size decreased the most in the thinnest pinches, which experienced most of the deformation; and (9) in the highly thinned pinch the deformation mechanism has changed, at some stage, from dislocation creep dominated to diffusion creep dominated. This interpretation only considers the layer extension, which most likely was dominated by the pure shearing.

A good understanding of processes and behaviors during ductile deformation enables the use of observed structures to infer (1) deformation history (e.g. amount of strain, pure or simple shear etc.) and (2) paleo-rheology (e.g. linear or non-linear viscous, viscosity ratio, softening mechanism active or not etc., e.g. Passchier et al., 1993; Kenis et al., 2004). Hence, if the formation of pinch-and-swell structure for small viscosity ratio involves material softening, then pinch-and-swell structure can be used to infer past material softening. A number of workers have inferred such a relationship (e.g. Neurath and Smith, 1982; Rutter, 1998; Hobbs et al., 2010). However, our numerical simulations show that material softening, such as strain and strain-rate softening, is not necessary for pinch-and-swell formation, even for small viscosity ratios. Low-temperature plasticity is another behavior that can

Fig. 10. a) EBSD inverse pole figure (IPF) map of the interior of the swell of a calcite vein similar to Fig. 9 and from the same location. The large grains have been toned up to better image the small grains that developed between them. Parallel bands of small grains develop inside the large grains, dividing them in several subparts. These bands can be both oblique and parallel to the twins. The twins of the large grains are slightly bent. b) Misorientation gradient map with reference orientations in the host domain I, the twin domain II (twins oriented from low-left to up-right) and twin domain III (twins oriented from up-left to low-right) of the large grain. The large grains show strong intergranular misorientation of more than 30°. The oblique bands of small grains that divide the large grain into subparts indicate limits of strong misorientation inside the large grain. In both maps, black lines are high angle boundaries (>10°, see text for detailed description). The three larger circles in b) are zooms to better image examples of bulging recrystallization (BLG) and subgrain rotation (SR).

cause formation of pinch-and-swell structure for small values of *R*. Therefore, the question as to whether observed pinch-and-swell structure was generated by a fluid dynamic instability during viscoplastic flow or softening behavior cannot be answered by the presence of the pinch-and-swell structure itself. More observations are needed to evaluate the deformation behavior for each pinch-and-swell structure. For example, Renner et al. (2002) published a flow law for dislocation creep of calcite that can exhibit large effective stress exponents and is also dependent on grain size. This grain size dependence can cause softening due to grain size reduction. The quantification of the relative importance of plasticity (i.e. large effective stress exponent) versus softening requires more observations and mathematical analysis.

A mechanism that can also cause and significantly increase the necking instability is viscous strain heating. This thermodynamic feed-back mechanism is well studied (e.g. Schubert and Yuen, 1978; Brun and Cobbold, 1980; Regenauer-Lieb and Yuen, 1998; Kaus and Podladchikov, 2006; Braeck et al., 2009), but its involvement in tectonic deformation and geological structures has mainly focused on large-scale ductile structures (say layer thickness >100 m, e.g. Hobbs et al., 2007; Burg and Schmalholz, 2008; Schmalholz et al., 2009) rather than small-scale systems, such as layers with thicknesses of 1–10 cm. Recent studies, however, suggest that viscous strain heating can also be important on the small-scale if viscoelastic stress relaxation and high initial stresses are considered (Braeck and Podladchikov, 2007; John et al., 2009).

Most viscously deformed rocks with layer-parallel shortening exhibit folds. A well developed and continuous pinch-and-swell structure is not as common in rock with layer-parallel extension, so that pinch-and-swell structure seems to be less abundant than buckle-folds, which is a contention based only on the authors' personal experience during field work. The lesser abundance of pinch-and-swell structure is plausible mainly because of two reasons: (1) the formation of pinch-and-swell structure requires large effective stress exponents and/or material softening, whereas the formation of folds does not; and (2) for multilayers, initial pinch-and-swell formation can be replaced by shear zone formation, whereas multilayer folding is usually not replaced by another style of deformation.

6. Conclusions

The von Mises plasticity is used to model low-temperature plasticity for dislocation glide. Rock deformation in the low-temperature plasticity regime usually exhibits a significantly weaker stress dependence on strain-rate than in the dislocation creep regime. Therefore, effective (or apparent) power-law stress exponents are significantly larger than 10 for flow laws applicable in the low-temperature plasticity regime.

Pinch-and-swell structure can form in a viscoplastic layer exhibiting a power-law flow law and a von Mises yield stress for small reference viscosity ratios between layer and viscous matrix (10–20) and small power-law stress exponents (1–5). Both the power-law flow law and the von Mises plasticity do not require material softening. Therefore, material softening, such as for example strain-rate softening, is not essential for the formation of pinch-and-swell structure. Consequently, detailed microstructural observations are necessary to determine the role of material softening during pinch-and-swell formation. For example, microstructural observations and EBSD data for a set of calcite veins indicate that the deformation during pinch-and-swell formation was dominated by dislocation glide and low-temperature grain-boundary migration, which are processes of the low-temperature plasticity regime. Therefore, material softening likely played a minor role during the formation of the observed pinch-and-swell structure.

The numerical simulations for initial random geometrical perturbations show that pinches and individual boudins do not need to develop simultaneously. Individual boudins with larger aspect ratios are continuously stressed during bulk extension due to shear coupling with the matrix and additional pinches can form in their centers. Simulations of multilayer pinch-and-swell structure show that pinches can form on different scales, i.e. the scale of the individual layer and the scale of the multilayer. The multilayer simulations also show the development of shear zones that exhibit significant displacement. This shear zone formation is a true multilayer effect for the applied model set-up because such shear zones did not develop in the single-layers. The basic features of the numerical simulations, such as (1) strongly varying distances between individual boudins, (2) not fully developed pinches within individual boudins and (3) shear zones with normal drag geometry in multilayers, are also observable in nature.

Pinches developed during pure shear extension in the simulations with single layers. These pinches resulted from a necking instability and represent one mode of strain localization. In the simulations with multilayers, shear zones developed due to the oblique linkage of pinches across the multilayer. These simulations can explain strain localization by shear zone formation during bulk pure shear extension of viscoplastic multilayers without any material softening or feed-back mechanism (e.g. shear heating).

Acknowledgments

Reviews by B. Grasemann and P. Bons and by editor W. Dunne are gratefully acknowledged. This work was supported by the University of Lausanne.

References

Barnhoorn, A., Bystricky, M., Burlini, L., Kunze, K., 2004. The role of recrystallisation on the deformation behaviour of calcite rocks: large strain torsion experiments on Carrara marble. Journal of Structural Geology 26 (5), 885–903.

Batchelor, G.K., 1967. An Introduction to Fluid Dynamics. Cambridge University Press, Cambridge.

Bestmann, M., Prior, D.J., 2003. Intragranular dynamic recrystallization in naturally deformed calcite marble: diffusion accommodated grain boundary sliding as a result of subgrain rotation recrystallization. Journal of Structural Geology 25 (10), 1597–1613.

Brack, P., 1981. Structures in the southwestern border of the Adamello intrusion (Alpi Bresciane, Italy). Schweizerische Mineralogische und Petrographische Mitteilungen 61, 37–50.

Brack, P., 1985. Multiple intrusions – examples from the Adamello batholith (Italy) and their significance on the mechanisms of intrusion. Memorie della Società Geologica Italiana 26, 145–157.

Braeck, S., Podladchikov, Y.Y., 2007. Spontaneous thermal runaway as an ultimate failure mechanism of materials. Physical Review Letters 98 (9).

Braeck, S., Podladchikov, Y.Y., Medvedev, S., 2009. Spontaneous dissipation of elastic energy by self-localizing thermal runaway. Physical Review E 80 (4).

Brun, J.P., Cobbold, P.R., 1980. Strain heating and thermal softening in continental shear zones – a review. Journal of Structural Geology 2 (1–2), 149–158.

Burg, J.P., Schmalholz, S.M., 2008. Viscous heating allows thrusting to overcome crustal-scale buckling: numerical investigation with application to the Himalayan syntaxes. Earth and Planetary Science Letters 274, 189–203.

Burkhard, M., 1993. Calcite twins, their geometry, appearance and significance as stress–strain markers and indicators of tectonic regime – a review. Journal of Structural Geology 15 (3–5), 351–368.

Carter, N.L., Tsenn, M.C., 1987. Flow properties of continental lithosphere. Tectonophysics 136, 27–63.

Cuvelier, C., Segal, A., van Steenhoven, A.A., 1986. Finite Element Methods and the Navier-Stokes Equations. D. Reidel Publishing Company.

Dabrowski, M., Krotkiewski, M., Schmid, D.W., 2008. MILAMIN: MATLAB-based finite element method solver for large problems. Geochemistry, Geophysics, Geosystems 9.

Davis, N.E., Kronenberg, A.K., Newman, J., 2008. Plasticity and diffusion creep of dolomite. Tectonophysics 456 (3–4), 127–146.

De Bresser, J.H.P., 2002. On the mechanism of dislocation creep of calcite at high temperature: inferences from experimentally measured pressure sensitivity and strain rate sensitivity of flow stress. Journal of Geophysical Research-Solid Earth 107 (B12).

De Bresser, J.H.P., Spiers, C.J., 1990. High-temperature Deformation of Calcite Single-crystals by R+ and F+ Slip.

De Bresser, J.H.P., Spiers, C.J., 1993. Slip systems in calcite single-crystals deformed at 300–800 degrees C. Journal of Geophysical Research-Solid Earth 98 (B4), 6397–6409.
Dorner, D., Stockhert, B., 2004. Plastic flow strength of jadeite and diopside investigated by microindentation hardness tests. Tectonophysics 379 (1–4), 227–238.
Emerman, S.H., Turcotte, D.L., 1984. A back-of-the-envelope approach to boudinage mechanics. Tectonophysics 110 (3–4), 333–338.
Goetze, C., 1978. Mechanisms of creep in olivine. Philosophical Transactions of the Royal Society of London Series A-Mathematical Physical and Engineering Sciences 288 (1350), 99–119.
Grasemann, B., Martel, S., Passchier, C., 2005. Reverse and normal drag along a fault. Journal of Structural Geology 27 (6), 999–1010.
Grasemann, B., Stuwe, K., Vannay, J.C., 2003. Sense and non-sense of shear in flanking structures. Journal of Structural Geology 25 (1), 19–34.
Gratier, J.P., Guiguet, R., Renard, F., Jenatton, L., Bernard, D., 2009. A pressure solution creep law for quartz from indentation experiments. Journal of Geophysical Research-Solid Earth 114.
Herwegh, M., Pfiffner, O.A., 2005. Tectono-metamorphic evolution of a nappe stack: a case study of the Swiss Alps. Tectonophysics 404 (1–2), 55–76.
Hirth, G., Tullis, J., 1992. Dislocation creep regimes in quartz aggregates. Journal of Structural Geology 14 (2), 145–159.
Hobbs, B., Regenauer-Lieb, K., Ord, A., 2007. Thermodynamics of folding in the middle to lower crust. Geology 35 (2), 175–178.
Hobbs, B.E., Ord, A., Spalla, M.I., Gosso, G., Zucali, M., 2010. The interaction of deformation and metamorphic reactions. In: Spalla, M.I., Marotta, A.M., Gosso, G. (Eds.), Advances in Interpretation of Geological Processes: Refinement of Multi-scale Data and Integration in Numerical Modelling. Geological Society, London, Special Publications, vol. 332, pp. 189–223. London.
Hudleston, P.J., Treagus, S.H., 2010. Information from folds: a review. Journal of Structural Geology 32, 2042–2071.
John, T., Medvedev, S., Rupke, L.H., Andersen, T.B., Podladchikov, Y.Y., Austrheim, H., 2009. Generation of intermediate-depth earthquakes by self-localizing thermal runaway. Nature Geoscience 2 (2), 137–140.
Johnson, A.M., Fletcher, R.C., 1994. Folding of Viscous Layers. Columbia University Press, New York.
Kaus, B.J.P., Podladchikov, Y.Y., 2006. Initiation of localized shear zones in viscoelastoplastic rocks. Journal of Geophysical Research-Solid Earth 111 (B4).
Kenis, I., Urai, J., vanderZee, W., Sintubin, M., 2004. Mullions in the High-Ardenne Slate Belt (Belgium): numerical model and parameter sensitivity analysis. Journal of Structural Geology 9 (26), 1677–1692.
Kirby, S.H., Kronenberg, A.K., 1984. Deformation of clinopyroxenite – evidence for a transition in flow mechanisms and semibrittle behavior. Journal of Geophysical Research 89 (NB5), 3177–3192.
Kohlstedt, D.L., 2007. Properties of rocks and minerals – constitutive equations, rheological behavior, and viscosity of rocks. In: Schubert, G. (Ed.), Treatise on Geophysics. Elsevier, pp. 389–417.
Lemiale, V., Muhlhaus, H.B., Moresi, L., Stafford, J., 2008. Shear banding analysis of plastic models formulated for incompressible viscous flows. Physics of the Earth and Planetary Interiors 171 (1–4), 177–186.
Montesi, L.G.J., Zuber, M.T., 2002. A unified description of localization for application to large-scale tectonics. Journal of Geophysical Research 107. doi:10.1029/2001JB000465.
Neurath, C., Smith, R.B., 1982. The effect of material properties on growth rates of folding and boudinage: experiments with wax models. Journal of Structural Geology 4, 215–229.
Passchier, C.W., Tenbrink, C.E., Bons, P.D., Sokoutis, D., 1993. Delta-objects as a gauge for stress sensitivity of strain-rate in mylonites. Earth and Planetary Science Letters 120 (3–4), 239–245.
Passchier, C.W., Trouw, R.A.J., 2005. Microtectonics. Springer, Berlin.
Pollard, D.D., Fletcher, R.C., 2005. Fundamentals of Structural Geology. Cambridge University Press, Cambridge.
Price, N.J., Cosgrove, J.W., 1990. Analysis of Geological Structures. Cambridge University Press, Cambridge.
Ramberg, H., 1955. Natural and experimental boudinage and pinch-and-swell structures. Journal of Geology 63 (6), 512.
Regenauer-Lieb, K., Yuen, D.A., 1998. Rapid conversion of elastic energy into plastic shear heating during incipient necking of the lithosphere. Geophysical Research Letters 25 (15), 2737–2740.
Renner, J., Evans, B., 2002. Do calcite rocks obey the power-law creep equation? In: DeMeer, S., Drury, M.R., DeBresser, J.H.P., Pennock, G.M. (Eds.), Deformation Mechanisms, Rheology and Tectonics: Current Status and Future Perspectives Geological Society Special Publication, vol. 200, pp. 293–307.
Renner, J., Evans, B., Siddiqi, G., 2002. Dislocation creep of calcite. Journal of Geophysical Research-Solid Earth 107 (B12).
Renner, J., Siddiqi, G., Evans, B., 2007. Plastic flow of two-phase marbles. Journal of Geophysical Research-Solid Earth 112 (B7).
Rutter, E.H., 1976. Kinetics of rock deformation by pressure solution. Philosophical Transactions of the Royal Society of London Series A-Mathematical Physical and Engineering Sciences 283 (1312), 203–219.
Rutter, E.H., 1998. Use of extension testing to investigate the influence of finite strain on the rheological behaviour of marble. Journal of Structural Geology 20 (2–3), 243–254.
Rybacki, E., Dresen, G., 2004. Deformation mechanism maps for feldspar rocks. Tectonophysics 382 (3–4), 173–187.
Schmalholz, S.M., 2006. Scaled amplification equation: a key to the folding history of buckled viscous single-layers. Tectonophysics 419 (1–4), 41–53.
Schmalholz, S.M., Fletcher, R.C., 2011. The exponential flow law applied to necking and folding of a ductile layer. Geophysical Journal International 184, 83–89.
Schmalholz, S.M., Kaus, B.J.P., Burg, J.-P., 2009. Stress-strength relationship in the lithosphere during continental collision. Geology 37 (9), 775–778.
Schmalholz, S.M., Podladchikov, Y.Y., Jamtveit, B., 2005. Structural softening of the lithosphere. Terra Nova 17, 66–72.
Schmalholz, S.M., Schmid, D.W., Fletcher, R.C., 2008. Evolution of pinch-and-swell structures in a power-law layer. Journal of Structural Geology 30, 649–663.
Schmid, S.M., Paterson, M.S., Boland, J.N., 1980. High-temperature flow and dynamic recrystallization in Carrara marble. Tectonophysics 65 (3–4), 245–280.
Schubert, G., Yuen, D.A., 1978. Shear heating instability in earths upper mantle. Tectonophysics 50 (2–3), 197–205.
Shewchuk, J.R., 2002. Delaunay refinement algorithms for triangular mesh generation. Computational Geometry-Theory and Applications 22 (1–3), 21–74.
Smith, R.B., 1977. Formation of folds, boudinage, and mullions in non-Newtonian materials. Geological Society of America Bulletin 88 (2), 312–320.
Stipp, M., Stunitz, H., Heilbronner, R., Schmid, S.M., 2002. The eastern Tonale fault zone: a 'natural laboratory' for crystal plastic deformation of quartz over a temperature range from 250 to 700 degrees C. Journal of Structural Geology 24 (12), 1861–1884.
Tsenn, M.C., Carter, N.L., 1987. Upper limits of power law creep of rocks. Tectonophysics 136 (1–2), 1–26.
Turcotte, D.L., Schubert, G., 1982. Geodynamics. Applications of Continuum Physics to Geological Problems. John Wiley & Sons, New York.
White, S.H., 1976. The role of dislocation processes during tectonic deformation with special reference to quartz. In: Strens, R.J. (Ed.), The Physics and Chemistry of Minerals and Rocks. Wiley, London, pp. 75–91.
Yarushina, V.M., Dabrowski, M., Podladchikov, Y.Y., 2010. An analytical benchmark with combined pressure and shear loading for elastoplastic numerical models. Geochemistry, Geophysics, Geosystems 11 (8).